Original Article

An automatic deep learning-based bone mineral density measurement method using X-ray images of children

Hongye Zhao[1,2#], Yi Zhang[1,2#], Wenshuang Zhang[3,4#], Ling Wang[3,5], Kai Li[3], Jian Geng[3], Xiaoguang Cheng[3,4,6], Tongning Wu[1,2]

[1]China Academy of Information and Communications Technology, Beijing, China; [2]Key Laboratory of Artificial Intelligence Key Technologies and Applications Evaluation, Ministry of Industry and Information Technology, Beijing, China; [3]Department of Radiology, Beijing Jishuitan Hospital, Capital Medical University, Beijing, China; [4]Department of Radiology, Peking University Fourth School of Clinical Medicine, Beijing, China; [5]JST Sarcopenia Research Centre, National Center for Orthopaedics, Beijing Research Institute of Traumatology and Orthopaedics, Beijing Jishuitan Hospital, Capital Medical University, Beijing, China; [6]Beijing Research Institute of Traumatology and Orthopaedics, Beijing, China

Contributions: (I) Conception and design: H Zhao, Y Zhang, W Zhang, X Cheng, T Wu; (II) Administrative support: X Cheng, T Wu; (III) Provision of study materials or patients: W Zhang, L Wang, K Li, J Geng, X Cheng; (IV) Collection and assembly of data: W Zhang, L Wang, K Li, J Geng, X Cheng; (V) Data analysis and interpretation: H Zhao, Y Zhang, T Wu; (VI) Manuscript writing: All authors; (VII) Final approval of manuscript: All authors.

[#]These authors contributed equally to this work.

Correspondence to: Xiaoguang Cheng, MD. Department of Radiology, Beijing Jishuitan Hospital, Capital Medical University, No. 31 Xinjiekou East Street, Beijing 100035, China; Department of Radiology, Peking University Fourth School of Clinical Medicine, Beijing, China; Beijing Research Institute of Traumatology and Orthopaedics, Beijing, China. Email: xiao65@263.net; Tongning Wu, PhD. China Academy of Information and Communications Technology, No. 52, Huayuanbei Road, Beijing 100191, China; Key Laboratory of Artificial Intelligence Key Technologies and Applications Evaluation, Ministry of Industry and Information Technology, Beijing, China. Email: wutongning@caict.ac.cn.

Background: Osteoporosis is a common bone disease characterized by low bone mineral density (BMD). Low BMD screening and early interventions during childhood can significantly decrease osteoporosis risk in adulthood. However, in clinical settings, the applicability of dual-energy X-ray absorptiometry (DXA), a technique to measure standard area BMD (aBMD), cannot adequately meet the diagnostic needs of the majority of the Chinese population. We aimed to achieve a comprehensive evaluation in clinical settings by taking a single X-ray image, which, in conjunction with the use of equivalent step phantoms, can assess bone age or injuries (such as sprains, fractures, or breaks) in the wrist while also measuring aBMD in the forearm, to further evaluate growth and development.

Methods: In the present study, we used routine X-ray images of the hand and forearm to measure aBMD with step phantom. First, based on the X-ray images, the regions of interest (ROIs) and step phantom used in clinical settings were automatically located and segmented; then, their average grayscale values were calculated. Second, after fitting the linear calibration relationship between the equivalent phantom thickness and grayscale value of the phantom, the effect of soft tissue on aBMD measurement was eliminated using a deep learning method. Finally, aBMD was measured.

Results: Our developed method was validated on 500 X-ray images taken at the clinic and compared with DXA-based aBMD measurements. Experiments revealed that the average correlation coefficient was 0.836.

Conclusions: The proposed method is an automatic method for measuring aBMD in children by utilizing X-ray images of hand and forearm. Furthermore, our findings suggest the effectiveness of the developed method, which provides a comparable performance to that of clinicians.

Keywords: Deep learning; bone mineral density (BMD); key point localization; image processing

Submitted Feb 13, 2024. Accepted for publication Dec 02, 2024. Published online Feb 11, 2025.
doi: 10.21037/qims-24-283
View this article at: https://dx.doi.org/10.21037/qims-24-283

Introduction

Low bone mineral density (BMD) during childhood can result in various negative outcomes, including osteoporosis, and an increased risk of cervical and lumbar hyperplasia. These outcomes may subsequently result in the impaired growth and development of children. The skeletal health status throughout life is affected by skeletal development during childhood and adolescence (1). Therefore, accurately evaluating a child's bone density is crucial for assessing normal growth and development, identifying deviations, detecting bone mass deficiencies due to insufficient activity and nutrition, as well as recognizing secondary osteoporosis caused by underlying diseases and medications. In this context, it is also of paramount importance to assess and monitor BMD in children for early identification and intervention of potential skeletal health issues.

Area BMD (aBMD) and volumetric BMD (vBMD) can be used to characterize BMD. In pediatric bone density assessment, choosing aBMD over vBMD is primarily related to the practicality and relevance of the measurement techniques for growing bones. aBMD, measured via dual-energy X-ray absorptiometry (DXA) (2), is more suitable for children due to its two-dimensional assessment, which is effective for accessing bones that are still developing and changing in size and shape. This method aligns with the characteristics of rapid and uneven growth patterns of childhood. On the other hand, vBMD, typically measured through more complex and less accessible modalities like quantitative computed tomography (QCT) (3), which are more suitable for accessing stable, fully developed adult bones, can provide three-dimensional insights (4). In children, whose bones are rapidly growing and remodeling, aBMD provides accurate and reliable data for clinical assessment, making it an important parameter for both clinical practice and research (5). Therefore, in the present study, we selected aBMD as the evaluation metric.

At present, DXA (6,7), QCT (8), and X-ray imaging (9,10) are the most commonly used methods to measure aBMD in clinical settings. However, multiple factors should be considered when applying these imaging techniques in clinical settings, including cost, radiation dose, and accuracy. DXA measures the density of different structures by determining the energy difference after the penetration of X-rays in the bones and soft tissues. The Pediatric Task Force of the International Society for Clinical Densitometry (ISCD) recommends DXA for measuring aBMD in the posterior-anterior lumbar spine and total body less head (TBLH) areas in most pediatric patients as an important component of comprehensive bone health assessment in pediatric and adolescent patients with conditions known or suspected to increase skeletal fragility (11). However, access to the DXA examinations varies geographically and is often insufficient. In China, it cannot adequately meet the diagnostic needs of the majority of the Chinese population (12). In addition, the population coverage and radiation dose of QCT-based screening strategies are barriers to their use in clinical settings (13). QCT is generally used as an opportunistic screening for adults in the routine physical examination population, yet opportunistic scanning for children is relatively rare. Moreover, the radiation dose of QCT is relatively large, which may limit its clinical application in long-term BMD measurement in children.

Previous studies (9,10) have revealed the potential of using hand X-ray images for measuring aBMD. First, the ISCD also noted that other skeletal sites may be useful depending on the clinical need. The forearm, as the alternative site, may be used for DXA measurements under circumstances when other standard sites cannot be measured safely, accurately, or without artifact interference (11). In particular, studies have demonstrated that forearm aBMD measurements can effectively predict major osteoporotic fractures (14) and the risk of wrist and forearm fractures (15). More importantly, the single image taken with the forearm and the equivalent step phantom can be used to assess bone age or injuries (such as sprains, fractures, or breaks) in the wrist while also measuring aBMD in the forearm, thereby decreasing time, costs, and radiation risk, with particular benefits for children.

Inspired by these advantages, researchers have analyzed and compared aBMD derived from X-ray imaging and DXA and noted a relatively good correlation (correlation coefficient =0.79) for aBMD measurements using fingers (10). Subsequently, several studies have investigated the possibility of automatically measuring aBMD from X-ray images (16,17). Some studies have employed computed X-ray densitometry,

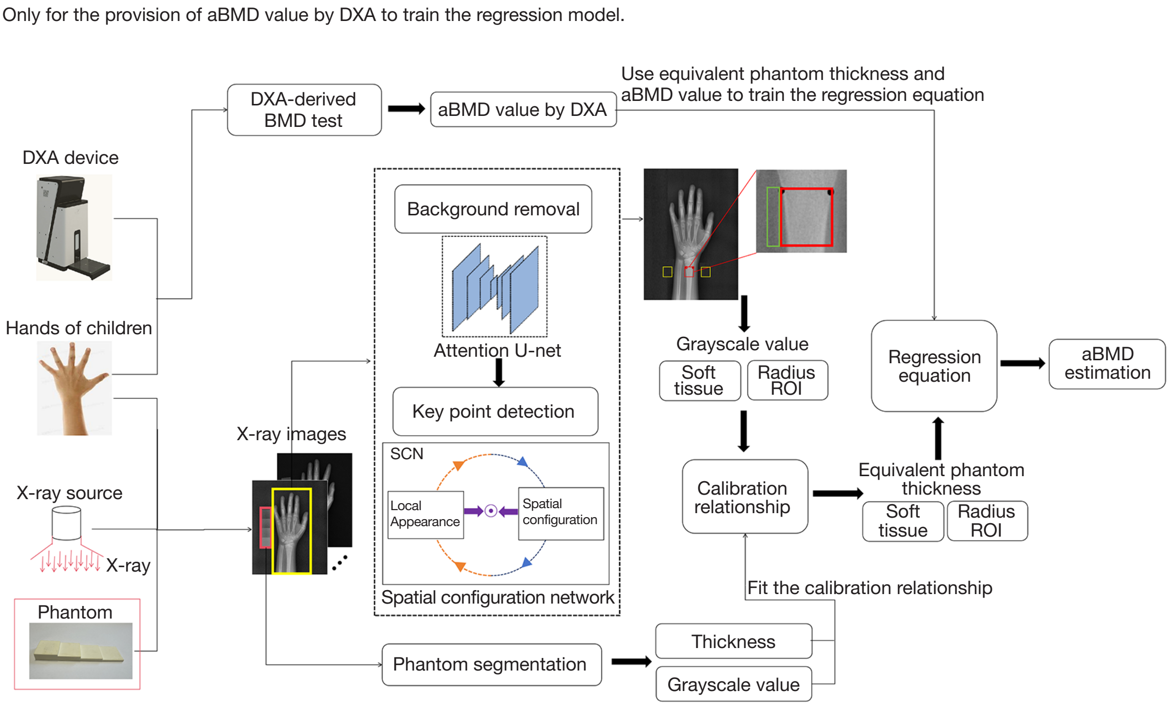

Figure 1 Study principle. This study constructed a dataset by collecting the aBMD of the forearm area measured using DXA and the X-ray images of the step phantom, the hand and forearm regions of children for model training. The parameters determined by training were used for aBMD measurement. The red box in the lower-left corner of the figure indicates the step phantom prepared using hydroxyapatite and soft tissue-equivalent epoxy resin. The phantom and hand are shown in the X-ray images as indicated by the red and yellow boxes. And after background subtraction, we specifically selected the background regions and the ROIs for the radius and soft tissue, as indicated by the yellow square (the background regions), red square (the ROI for the radius), and green square (the ROI for the soft tissue) outlines in the upper right X-ray image, respectively. aBMD, areal bone mineral density; DXA, dual X-ray absorptiometry; ROI, region of interest; SCN, spatial configuration network.

machine learning and deep learning methods to predict aBMD using metacarpal (18), and spinal X-ray images (19). These learning-based methods can identify and segment the regions of interest (ROIs) (20,21) and automatically classify and regress aBMD. However, studies on measuring forearm aBMD using the forearm (radius) X-ray images are lacking. In the relevant study, the ROIs were manually delineated from the forearm X-ray images of individuals over 25 years old and regressed for aBMD (22). However, the location of the ROIs was needed for manual delineation; furthermore, the study population was limited to adults, limiting its clinical application.

Considering the status quo of the research on aBMD, in the present study, we proposed a learning-based method to address these issues. First, X-ray images of the step phantom and the hand and forearm regions of children were used as imaging data. The effect of the X-ray device was eliminated by converting the grayscale values of the radius and soft tissues into equivalent phantom thickness. Second, a linear regression equation between aBMD via DXA and the equivalent phantom thickness was developed. Finally, aBMD was automatically measured. The experimental results on a clinical dataset of 500 images demonstrated a high correlation between aBMD via DXA and the measured values, indicating its potential for clinical promotion.

Methods

Study principle

In this study, a fully automatic aBMD measurement procedure was implemented via three steps, as demonstrated in *Figure 1*. First, the attention U-Net algorithm was utilized to remove background interference, and the spatial configuration network (SCN) algorithm was utilized to segment the ROIs that were to be measured. The grayscale

Table 1 The characteristics of the participants

Parameters	Total	Kindergarten	Elementary school	Middle school
Sample size	500	37	233	230
Age (years)	11.75±3.84	4.49±0.83	10.23±2.57	14.47±2.66
Gender (male)	248 (49.60)	20 (54.10)	111 (47.64)	117 (50.87)
BMI (kg/m^2)	19.67±4.39	15.89±1.61	18.75±4.12	21.21±4.33

Data are presented as mean ± SD or n (%), unless otherwise stated. BMI, body mass index; SD, standard deviation.

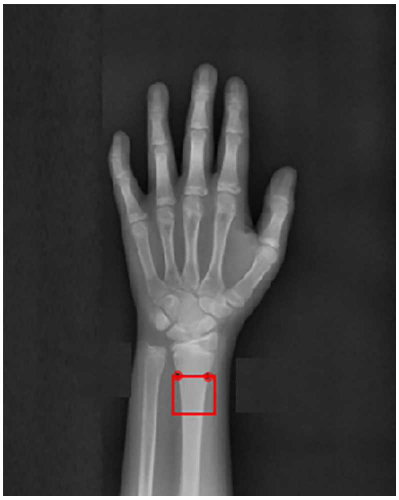

Figure 2 Example of the ROI segmentation of the radius (the selected area is outlined in red). ROI, region of interest.

values of the radius, adjacent soft tissues, and nearby background area were calculated. The grayscale values of the soft tissues and radius were corrected using those of the background area. Then, the phantom segmentation algorithm based on the template matching method was used to locate the grayscale values of each step in the step phantom automatically. A linear relationship was established between the grayscale values of X-ray images and the equivalent phantom thickness to obtain the equivalent phantom thicknesses of the radius and soft tissues. Finally, using a learning-based method, the linear regression equation between the aBMD via DXA and the equivalent phantom thicknesses of the radius and soft tissues on the selected measurement position was established, and the aBMD value was obtained from the X-ray images.

Data acquisition

This study was conducted according to the principles of the Declaration of Helsinki (as revised in 2013). The survey was reviewed and approved by the Ethics Committee of Beijing Jishuitan Hospital (No. 201907-11). The participants were healthy school children aged 3–16 years who volunteered to participate in the study and had received parental consent. The characteristics of the participants are detailed in *Table 1*. The participants underwent X-ray imaging of the left hand and a part of the forearm in the Beijing Jishuitan Hospital, as well as an examination of the forearm area using DXA. In total, the dataset comprised 500 X-ray images selected from 749 clinical images based on their quality. These images were resized to 2,048×2,560.

A table-mounted digital X-ray device (Xbone, Dymena Healthcare, Shanghai, China) was used to acquire the X-ray images of all participants. The imaging parameters of the X-ray device were as follows: 75 kVp, 200 µA, imaging area of 300 mm × 300 mm (image resolution: 0.12 mm pixel), and focus-film distance of 100 cm. aBMD was assessed using peripheral DXA with an EXA-3000 instrument (Osteosys, Seoul, Korea).

A four-step thickness phantom prepared using hydroxyapatite and soft tissue-equivalent epoxy resin (22), a material exhibiting X-ray attenuation characteristics similar to the bones, was imaged along with the left forearm as shown in *Figure 1*. The phantom and the wrist were imaged simultaneously, with the phantom positioned approximately 2 to 3 cm from the edge of the wrist bone. Additionally, the grayscale value of phantom in the image was based on the thickness of the specific part of the phantom. Because the phantom thickness was known, the relationship between the thickness and grayscale value could be derived (23,24). Therefore, this relationship was utilized to determine the equivalent phantom thickness of the ROI and soft tissues.

Data preprocessing

Based on the clinical procedures, ROI for measuring the forearm aBMD was defined as the region between both

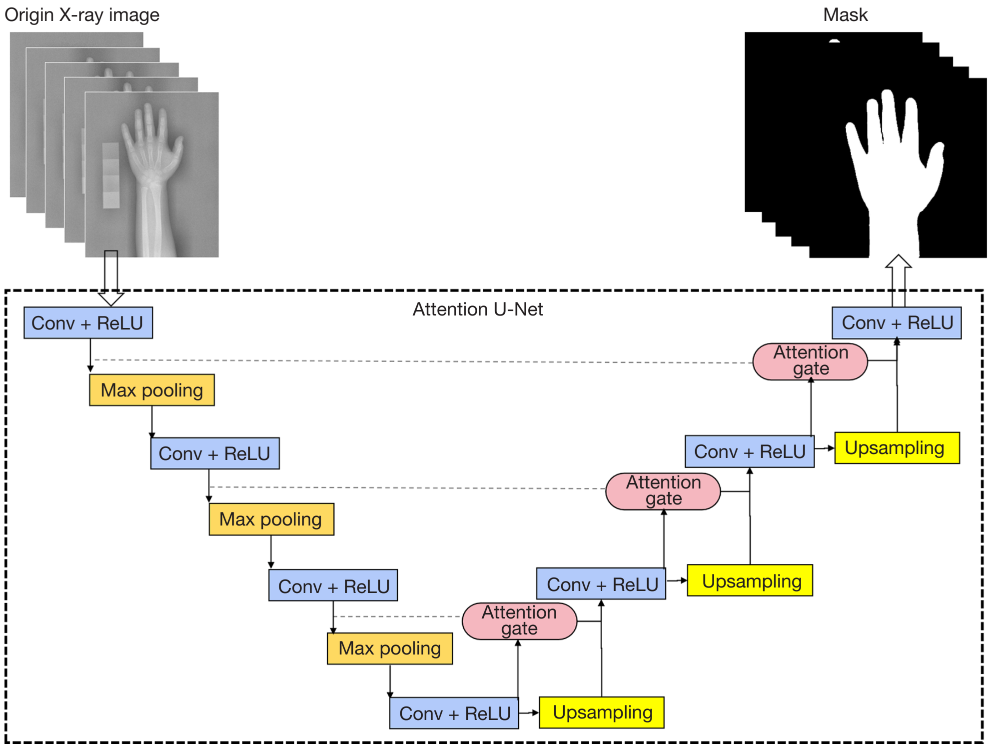

Figure 3 Background removal procedure. Conv, convolution; ReLU, rectified linear unit.

ends of the distal tightening of the radius [most studies select the ultra-distal radius and one-third of the radius (15,25)], because it is the high-risk area for forearm and wrist fractures (*Figure 2*). Therefore, the background should be removed, and the aforementioned region should be accurately selected.

Background removal

Before locating the ROI, the hand and phantom regions were identified. In this study, attention U-Net (26), a variant of U-Net (27), was used. In this algorithm, an attention module was integrated into the traditional U-Net architecture to enhance the sensitivity of identifying foreground pixels in the image by highlighting the features of specific areas. In the encoding part of the network, every input image was progressively filtered and downsampled by factor of 2 at each scale. Attention gates filtered the features propagated through the skip connections. Feature selectivity in attention gates was achieved by using contextual information extracted in coarser scales. Finally, the attention U-Net network used in this method could automatically learn the target structures of different shapes and sizes, and extract the mask of the target area from the original X-ray image to remove the background. *Figure 3* illustrates the procedure for background removal.

Phantom segmentation

The phantom region was segmented using OpenCV via the template matching method. This method employs normalized squared difference {Eq. [1]} as the evaluation metric in matching. Optimal results are achieved when its value is zero:

$$R(x,y)=\frac{\sum_{x',y'}\left(T(x',y')-I(x+x',y+y')\right)^2}{\sqrt{\sum_{x',y'}T(x',y')^2\cdot\sum_{x',y'}I(x+x',y+y')^2}} \qquad [1]$$

Where $R(x,y)$ indicates the normalized squared difference value matched with the template of the area sized similar to the template, with (x,y) as the upper left corner on the original image; $T(x,y)$ and $I(x,y)$ indicate the grayscale values of the template image and the region on the original image, respectively; x' and y' indicate the process of traversing pixels on the template image; their values range from zero to the width or length of the template image.

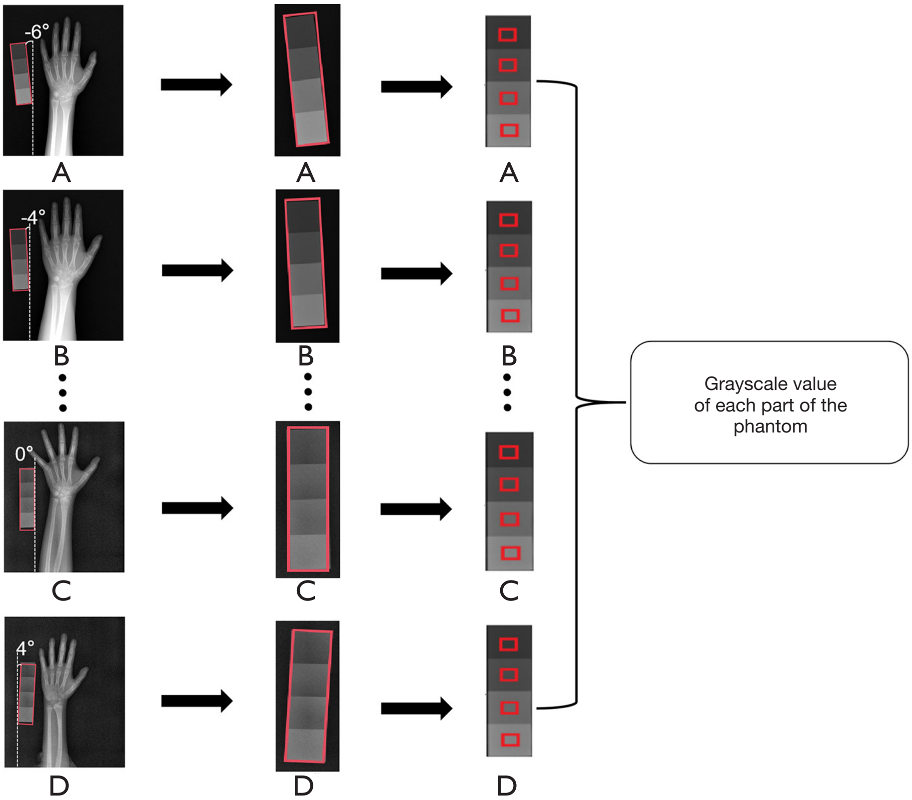

Figure 4 Addition of a rotational invariant factor to match and segment the phantoms at different angles. The average grayscale value of the boxed region was calculated. Phantoms rotated (A) −6°, (B) −4°, (C) 0°, and (D) 4° clockwise, respectively.

Because the position of the phantom may change during imaging, the template matching algorithm was improved by adding a rotational invariant factor, as demonstrated in *Figure 4*. For the phantom in the X-ray image captured at different angles, our developed method could accurately segment the actual edges and calculate the average grayscale values in the central area of each part. Furthermore, the experiments revealed that the phantom could be well-positioned and segmented from different angles.

The average grayscale value in the segmented phantom was calculated. Because the relationship between phantom thickness (unit: mm) and the grayscale value of the phantom could be highly linear over the range of the step phantom and the median correlation coefficient was r=0.9997 (22), we achieved the calibration relationship between the phantom thickness and grayscale value of the X-ray images via linear fitting to determine the parameters of the linear fitting equation. Before performing automated aBMD measurements, the calibration equation parameters were automatically calculated for each image, thereby establishing the relationship between the phantom thickness and grayscale value of that particular X-ray image.

Key point detection

In the context of this study, traditional location algorithms may provide inaccurate results owing to similarities in the texture of the radius in the X-ray images. Therefore, SCN (28) was developed for key point detection. This method can use the relative positions between different key points to correct and optimize the location results. In this method, the location task was converted into a heatmap regression task, achieving better performance with limited training data. SCN comprises two networks. The first sub-network was used to construct a feature-point heatmap. In the heatmap, the closer the key point, the higher the pixel grayscale value. The candidate prediction region located by this sub-network served as the input for the second sub-network. In the second sub-network, the spatial configuration component was introduced to improve the accuracy of the heatmap. Therefore, it could accurately provide the location coordinates of the key points.

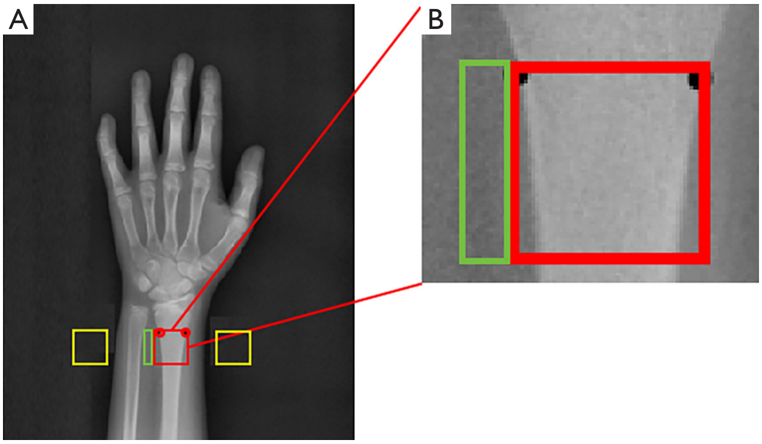

Figure 5 Regions for ROI extraction. (A) The selected bone and soft tissue ROIs and background areas in hand X-ray images. The yellow square indicates the background region. (B) Example of ROI segmentation for the radius (the selected area is outlined in red) and soft tissue (the selected area is outlined in green). ROI, region of interest.

ROI extraction

After the key points were located, the distal tightening of the radius and adjacent soft tissues was segmented via three steps. First, the ROI was segmented in the radial area. For the distal end of the radius, the line connecting those two key points aforementioned was used as one side to generate a square, as illustrated in *Figure 5* (the red square). Furthermore, by setting an adaptive threshold for grayscale values, the area outside the radius was removed. At this point, the ROI of the radius area was segmented. Second, the region of the soft tissue was segmented. A rectangle was chosen to delineate the soft tissue to eliminate the errors associated with the presence of the soft tissue (8), as illustrated in *Figure 5* (the green rectangle). Third, two square areas outside the wrist were extracted as the background region in the X-ray image, as illustrated in *Figure 5* (the yellow square).

After completing the segmentation, the average grayscale value of these areas was measured. The measurements of grayscale values over the ROIs and soft tissues were corrected for errors by subtracting the background measurements. Finally, using the linear calibration relationship mentioned above, the background-corrected data was converted into equivalent phantom thickness measurements.

Estimation of aBMD

After fitting the calibration relationship as mentioned above, aBMD was measured in two stages. During the training stage, forearm aBMD measurements via DXA and the equivalent step phantom thicknesses of the ROI and soft tissues were pooled and analyzed via linear regression analysis to elucidate the best fitting values of the coefficients P, Q, and R in Eq. [2] to eliminate the interference of soft tissue for X-ray image-based forearm aBMD measurement. During the test stage, the forearm aBMD in the X-ray images was calculated using Eq. [2], with values of the adjusted coefficients P, Q, and R determined from the training set mentioned above.

$$P \times \left(T\left(I_b\right) - Q \times T\left(I_t\right) \right) + R = aBMD_{DXA} \qquad [2]$$

where I_b indicates the average grayscale value of the ROI; I_t represents the average grayscale value of the soft tissue; T is the calibration relationship between the grayscale value and the equivalent phantom thickness; P (unit: g/cm^2/mm) indicates the relationship between the equivalent phantom thickness (unit: mm) and its corresponding aBMD measurement value (unit: g/cm^2); Q (unit: g/cm^2/mm) is the weight given to the equivalent phantom thickness of the soft tissue, representing its effect on the aBMD measurement value; and R is a constant term (unit: g/cm^2) used to improve the generalization of the equation. The values of parameters P and Q vary based on the different thicknesses of the radius and soft tissue.

Validation of the results

A five-fold cross-validation process was used. Five hundred images were randomly divided into five groups, with each

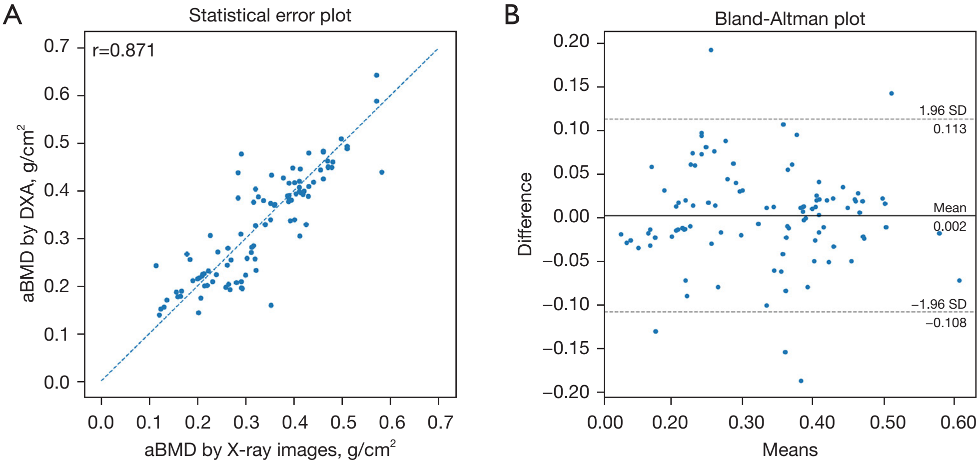

Figure 6 Best performance of the aBMD measurement in five-fold cross-validation. (A) Statistical error plot. (B) Bland-Altman plot. aBMD, areal bone mineral density; DXA, dual X-ray absorptiometry; r, the correlation coefficient; SD, standard deviation.

group alternating as the test set, whereas the remaining four groups were used as the training set.

To investigate the results of the ROI segmentation, four metrics were used: *Accuracy* {Eq. [3]}, *Dice* {Eq. [4]}, *IOU* {Eq. [5]}, and *Recall* {Eq. [6]}:

$$Accuracy = \frac{TP+TN}{TP+FP+FN+TN} \quad [3]$$

$$Dice = \frac{2\times\left|seg\cap \mathrm{Re}f\right|}{\left|Seg\right|+\left|\mathrm{Re}f\right|} \quad [4]$$

$$IOU = \frac{\left|seg\cap \mathrm{Re}f\right|}{\left|seg\cup \mathrm{Re}f\right|} \quad [5]$$

$$Recall = \frac{TP}{TP+FN} \quad [6]$$

where TP and FP indicate true positive pixels and false positive pixels, respectively; TN and FN indicate true negative pixels and false negative pixels, respectively; *Ref* denotes the actual segmentation results; and *Seg* denotes the segmentation results of our method.

To determine the performance of the key point location method, the point-to-point error based on Euclidean distance was used as the metric (28). For the key points in the image, the normalized point-to-point error is defined in Eq. [7]. The median, mean, and standard deviation (SD) of the point-to-point errors on all key points of all images were calculated as PE_{all}:

$$PE_{i}^{(j)} = \left\| \overset{*}{X}{}_{i}^{(j)} - \hat{X}_{i}^{(j)} \right\|_2 \quad [7]$$

To analyze the individual fitting results of the calibration relationship and the regression equation, as well as to evaluate the ROI segmentation results, correlation coefficient, a measure of the strength of the linear relationship between the two entities, was used. The formula for calculating this indicator is represented in Eq. [8]:

$$\mathbf{r} = \frac{E\left[\left(X-E\left[X\right]\right)\left(Y-E\left[Y\right]\right)\right]}{\sqrt{E\left[X-E\left[X\right]\right]^2}\sqrt{E\left[Y-E\left[Y\right]\right]^2}} \quad [8]$$

where X and Y indicate the two variables representing the predicted and actual values, respectively, and E is the expectation of this variable.

Results

aBMD measurement

Five-fold cross-validation was utilized to evaluate the linear regression equation for measuring aBMD. As described in the "Estimation of aBMD" section, the parameters in Eq. [2] were obtained from the training set, and the measured aBMD of the forearm using five test sets was compared with the forearm aBMD measurements via DXA. The average correlation coefficient was 0.836.

Figure 6 illustrates the statistical error plot and Bland-Altman plot. The obtained SD (0.056) was relatively small, and outliers exceeding the ±1.96 SD limit accounted for only 5% of all values, further proving performance consistency. Our results suggest that the proposed automatic forearm aBMD measurement method exhibits a

Table 2 Key point location results

Network	Image size (pixel)	PE_{all} (mm)		Outliers (>10 mm)
		Median	Mean ± SD	
SCN	1,024×1,024	0.38	0.46±0.51	4.6%

PE_{all}: the median, mean, and SD of the point-to-point errors on all key points of all images. SD, standard deviation; SCN, spatial configuration network.

Table 3 ROI segmentation results

Model	Accuracy	Dice	IOU	Recall rate
Attention U-Net	0.983	0.892	0.916	0.945
U-Net	0.961	0.855	0.881	0.917
Without the model	0.649	0.677	0.672	0.695

ROI, region of interest; IOU, intersection over union.

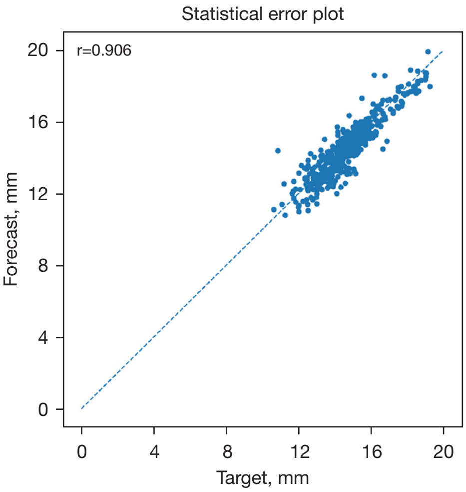

Figure 7 Scatter plot of the ROI segmentation results. r, the correlation coefficient; ROI, region of interest.

high correlation with the gold standard.

Key point location results

The locating performance of the SCN was investigated. The average results of all test images were evaluated, as summarized in *Table 2*. The median deviation radius of the outliers in network localization was 0.38 mm, the SD value of the deviation radius was 0.46±0.51 mm, and outliers with a localization error of more than 10 mm accounted for approximately 5% of all key points.

ROI segmentation results

Two sets of comparison experiments were performed for ROI segmentation: segmentation with and without the background removal model. *Table 3* summarizes the segmentation results. The results suggest that the attention U-Net model can effectively improve the performance of the segmentation and the fineness of edge segmentation.

Clinical doctors annotated the ROIs in the images and calculated their equivalent step phantom thickness. To validate the performance of ROI segmentation, the equivalent step phantom thickness of the ROIs was calculated using the entire dataset; these values were then compared with those calculated by doctors. *Figure 7* illustrates the error statistics. The correlation coefficient between both entities was 0.906. These results suggest that ROI segmentation was performed at a competence level comparable with that of clinicians.

Discussion

In this study, we proposed an automated method to measure forearm aBMD using X-ray images. Using this method, the key points for ROI segmentation were located, regression analysis was employed to eliminate the effect of soft tissues, and aBMD was measured. Our proposed method is suitable for aBMD measurement in children because it only requires a single X-ray image to be taken of the forearm with the equivalent step phantom. This single image can assess bone age or injuries (such as sprains, fractures, or breaks) in the wrist while also measuring aBMD in the forearm. This approach reduces additional costs and radiation exposure while providing a more comprehensive evaluation of children's growth and development. Additionally, the method increases attention to the risk of forearm fractures in athletic children.

The experimental results revealed a strong correlation between aBMD from X-ray imaging and that from DXA (r=0.836), suggesting the clinical relevance of the hand

Table 4 Comparison of key point location network results

Network	Image size (pixel)	PE_{all} (mm)		Outliers (>10 mm)
		Median	Mean ± SD	
SCN	1,024×1,024	0.38	0.46±0.51	4.60%
Downsampling-Net	1,024×1,024	0.81	0.92±0.65	7.10%
ConvOnly-Net	1,024×1,024	0.62	0.77±0.72	6.60%
U-Net	1,024×1,024	0.47	0.54±0.62	5.20%

PE_{all}: the median, mean, and SD of the point-to-point errors on all key points of all images. SD, standard deviation; SCN, spatial configuration network.

and forearm X-ray image-based aBMD measurement method used in this study. Moreover, we observed a higher correlation compared with other similar studies (22). Furthermore, we successfully automated the entire aBMD measurement method.

The robustness and accuracy of the key point detection network significantly affected our proposed aBMD measurement method. Therefore, we compared the location results of three other key point location networks: Downsampling-Net (29), ConvOnly-Net (29), and U-Net (27). Because SCN was based on heatmap regression, the number of network weights and computational complexity were decreased via image-to-image mapping. The performance of the four algorithms was determined; the results are summarized in *Table 4*. The SCN network achieved the best location results using the dataset. This further demonstrated the accuracy and reliability of the subsequent ROI segmentation.

Next, to eliminate the effect of background noise on key point detection, we used a segmentation algorithm for background removal. The attention U-Net network used in this method could automatically learn the target structures of different shapes and sizes. Furthermore, it enhanced the sensitivity of the model to the foreground objects of the images by highlighting the features of specific areas. The algorithm for background removal based on the attention U-Net network significantly improved all metrics, as demonstrated in *Table 3*.

Although we used an internal dataset for training and testing, our proposed method for estimating the aBMD of children using hand and forearm X-ray images holds promise for clinical application owing to two key reasons. First, the attention U-Net network used in the study can maximally eliminate the effects of differences in multicenter data that appear in forearm X-ray examinations in clinical settings because it is designed to handle datasets of different medical images. Second, the introduction of the calibration phantom allows the automatic establishment of the calibration relationship between aBMD and grayscale values in the X-ray images, considerably decreasing the effects of multicenter data. So, the method is worth for being promoted.

In the present study, we used images from children aged 3–16 years. Because children have various growth and developmental stages compared with adults, children of different age groups exhibit statistically significant differences in aBMD (22). Although there was a good correlation between the aBMD estimation results in our study, determining the parameters of the linear regression equation based on age group may further improve the results. In the future, we will collect more comprehensive data, including age, to differentiate the different parameters of the regression equation based on age groups.

With the widespread application of artificial intelligence technologies in medical image segmentation and biomedical signal processing tasks (30-32), the primary objective of this study was to apply the proposed automatic deep learning-based BMD measurement method in clinical settings for children undergoing bone age assessment and those who had experienced certain traumas. We aimed to take a single X-ray image, which, in conjunction with the use of equivalent step phantoms, can assess bone age or injuries in the wrist while also measuring aBMD in the forearm, to further evaluate growth and development. And this can reduce additional radiation exposure and imaging costs while improving measurement efficiency. Since our team has already made significant progress in the study of bone age assessment based on hand X-rays in children, and has published a series of research papers, as referenced (33,34). We plan to integrate the methods from both areas into software in the future, and the work on packaging the code and developing software for bone age studies has been basically completed.

Conclusions

We performed automatic clinical aBMD measurements using the forearm X-ray images of children. Using the method, key points were located and ROIs were extracted automatically. Furthermore, linear fitting and linear regression analysis, and a learning-based approach were used to remove the effects of soft tissues. The measured aBMD using X-ray images exhibited good consistency (0.836) with that using the gold standard (DXA), suggesting the accuracy of the proposed method. Simultaneously, the single image taken with the forearm and the equivalent step phantom can assess bone age or injuries (such as sprains, fractures, or breaks) in the wrist while also measuring aBMD in the forearm, thereby decreasing time, costs, and radiation risk, with particular benefits for children.

Acknowledgments

None.

Footnote

Funding: This research was funded by the National Natural Science Foundation of China (No. 62271508), the Beijing Hospitals Authority Clinical Medicine Development of Special Funding Support (No. ZYLX202107), the Beijing Municipal Health Commission (No. BJRITO-RDP-2024), the Guizhou Provincial Basic Research Program (Natural Science) (Qian Ke He Ji Chu-ZK[2022] General 450), and the Beijing Jishuitan Research Funding (No. XKDTR202316).

Conflicts of Interest: All authors have completed the ICMJE uniform disclosure form (available at https://qims.amegroups.com/article/view/10.21037/qims-24-283/coif). The authors have no conflicts of interest to declare.

Ethical Statement: The authors are accountable for all aspects of the work in ensuring that questions related to the accuracy or integrity of any part of the work are appropriately investigated and resolved. This study was conducted according to the principles of the Declaration of Helsinki (as revised in 2013). The survey was reviewed and approved by the Ethics Committee of Beijing Jishuitan Hospital (No. 201907-11). The participants were healthy school children aged 3–16 years who volunteered to participate in the study and had received parental consent.

References

1. Liu J, Wang L, Sun J, Liu G, Yan W, Xi B, Xiong F, Ding W, Huang G, Heymsfield S, Mi J. Bone mineral density reference standards for Chinese children aged 3-18: cross-sectional results of the 2013-2015 China Child and Adolescent Cardiovascular Health (CCACH) Study. BMJ Open 2017;7:e014542.
2. Mello JB, Rodríguez-Rodríguez F, Gracia-Marco L, Teodoro JL, Gaya AR, Gaya ACA. Speed, agility, and musculoskeletal fitness are independently associated with areal bone mineral density in children. Front Physiol 2023;14:1080091.
3. Liu Y, Wang L, Su Y, Brown K, Yang R, Zhang Y, Duanmu Y, Guo Z, Zhang W, Yan C, Yan D, Cheng X. CTXA hip: the effect of partial volume correction on volumetric bone mineral density data for cortical and trabecular bone. Arch Osteoporos 2020;15:50.
4. Chen L, Pan Y, Zhong F, Yuan TJ, Wang H, Chen T, Lv H, Cheng X, Liu JM, Lu Y. Using QCT to evaluate bone mineral and abdominal adipose changes in patients with primary hyperparathyroidism and comparing it to DXA for bone status assessment: a retrospective case-control study. Ann Transl Med 2022;10:606.
5. Engelke K, Lang T, Khosla S, Qin L, Zysset P, Leslie WD, Shepherd JA, Schousboe JT. Clinical Use of Quantitative Computed Tomography (QCT) of the Hip in the Management of Osteoporosis in Adults: the 2015 ISCD Official Positions-Part I. J Clin Densitom 2015;18:338-58.
6. Abrams SA; Committee on Nutrition. Calcium and vitamin d requirements of enterally fed preterm infants. Pediatrics 2013;131:e1676-83. Erratum in: Pediatrics 2024;154:e2024068306.
7. Faienza MF, D'Amato E, Natale MP, Grano M, Chiarito

M, Brunetti G, D'Amato G. Metabolic Bone Disease of Prematurity: Diagnosis and Management. Front Pediatr 2019;7:143.

8. Liu YC, Lin YC, Tsai PY, Iwata O, Chuang CC, Huang YH, Tsai YS, Sun YN. Convolutional Neural Network-Based Humerus Segmentation and Application to Bone Mineral Density Estimation from Chest X-ray Images of Critical Infants. Diagnostics (Basel) 2020.
9. Rosholm A, Hyldstrup L, Backsgaard L, Grunkin M, Thodberg HH. Estimation of bone mineral density by digital X-ray radiogrammetry: theoretical background and clinical testing. Osteoporos Int 2001;12:961-9.
10. Sotoca JM, Iñesta JM, Belmonte MA. Hand bone segmentation in radioabsorptiometry images for computerised bone mass assessment. Comput Med Imaging Graph 2003;27:459-67.
11. Weber DR, Boyce A, Gordon C, Högler W, Kecskemethy HH, Misra M, Swolin-Eide D, Tebben P, Ward LM, Wasserman H, Shuhart C, Zemel BS. The Utility of DXA Assessment at the Forearm, Proximal Femur, and Lateral Distal Femur, and Vertebral Fracture Assessment in the Pediatric Population: 2019 ISCD Official Position. J Clin Densitom 2019;22:567-89.
12. Cheng X, Yuan H, Cheng J, Weng X, Xu H, Gao J, Huang M, Wáng YXJ, Wu Y, Xu W, Liu L, Liu H, Huang C, Jin Z, Tian W; . Chinese expert consensus on the diagnosis of osteoporosis by imaging and bone mineral density. Quant Imaging Med Surg 2020;10:2066-77.
13. Hsieh CI, Zheng K, Lin C, Mei L, Lu L, Li W, Chen FP, Wang Y, Zhou X, Wang F, Xie G, Xiao J, Miao S, Kuo CF. Automated bone mineral density prediction and fracture risk assessment using plain radiographs via deep learning. Nat Commun 2021;12:5472.
14. Samelson EJ, Broe KE, Xu H, Yang L, Boyd S, Biver E, et al. Cortical and trabecular bone microarchitecture as an independent predictor of incident fracture risk in older women and men in the Bone Microarchitecture International Consortium (BoMIC): a prospective study. Lancet Diabetes Endocrinol 2019;7:34-43.
15. Miller PD, Siris ES, Barrett-Connor E, Faulkner KG, Wehren LE, Abbott TA, Chen YT, Berger ML, Santora AC, Sherwood LM. Prediction of fracture risk in postmenopausal white women with peripheral bone densitometry: evidence from the National Osteoporosis Risk Assessment. J Bone Miner Res 2002;17:2222-30.
16. Takada M, Engelke K, Hagiwara S, Grampp S, Jergas M, Glüer CC, Genant HK. Assessment of osteoporosis: comparison of radiographic absorptiometry of the phalanges and dual X-ray absorptiometry of the radius and lumbar spine. Radiology 1997;202:759-63.
17. Dendere R, Whiley SP, Douglas TS. Computed digital absorptiometry for measurement of phalangeal bone mineral mass on a slot-scanning digital radiography system. Osteoporos Int 2014;25:2625-30.
18. Matsumoto C, Kushida K, Yamazaki K, Imose K, Inoue T. Metacarpal bone mass in normal and osteoporotic Japanese women using computed X-ray densitometry. Calcif Tissue Int 1994;55:324-9.
19. Lee S, Choe EK, Kang HY, Yoon JW, Kim HS. The exploration of feature extraction and machine learning for predicting bone density from simple spine X-ray images in a Korean population. Skeletal Radiol 2020;49:613-8.
20. Zhang B, Yu K, Ning Z, Wang K, Dong Y, Liu X, et al. Deep learning of lumbar spine X-ray for osteopenia and osteoporosis screening: A multicenter retrospective cohort study. Bone 2020;140:115561.
21. Ho CS, Chen YP, Fan TY, Kuo CF, Yen TY, Liu YC, Pei YC. Application of deep learning neural network in predicting bone mineral density from plain X-ray radiography. Arch Osteoporos 2021;16:153.
22. Wang L, Huang P, Du H, Geng J, Yin X, Liu Y, Puri T, He B, Lyu L, Cheng X, Jiang X, Engelke K, Blake GM. Assessment of bone densitometry using radiography with a step-wedge phantom: a pilot study of the forearm. Quant Imaging Med Surg 2022;12:3340-50.
23. Pearson J, Ruegsegger P, Dequeker J, Henley M, Bright J, Reeve J, Kalender W, Felsenberg D, Laval-Jeantet AM, Adams JE. European semi-anthropomorphic phantom for the cross-calibration of peripheral bone densitometers: assessment of precision accuracy and stability. Bone Miner 1994;27:109-20.
24. Adams JE. Quantitative computed tomography. Eur J Radiol 2009;71:415-24.
25. Ma SB, Lee SK, An YS, Kim WS, Choy WS. The clinical necessity of a distal forearm DEXA scan for predicting distal radius fracture in elderly females: a retrospective case-control study. BMC Musculoskelet Disord 2023;24:177.
26. Schlemper J, Oktay O, Schaap M, Heinrich M, Kainz B, Glocker B, Rueckert D. Attention gated networks: Learning to leverage salient regions in medical images. Med Image Anal 2019;53:197-207.
27. Ronneberger O, Fischer P, Brox T. U-net: Convolutional networks for biomedical image segmentation. In: Medical Image Computing and Computer-Assisted Intervention-MICCAI 2015: 18th International Conference, Munich,

Germany, October 5-9, 2015, Proceedings, Part III 18. Cham: Springer International Publishing; 2015:234-41.
28. Payer C, Štern D, Bischof H, Urschler M. Integrating spatial configuration into heatmap regression based CNNs for landmark localization. Med Image Anal 2019;54:207-19.
29. Payer C, Štern D, Bischof H, Urschler M. Regressing heatmaps for multiple landmark localization using CNNs. In: International Conference on Medical Image Computing and Computer-Assisted Intervention. Cham: Springer International Publishing; 2016:230-8.
30. Xu X, Li C, Lan X, Fan X, Lv X, Ye X, Wu T. A Lightweight and Robust Framework for Circulating Genetically Abnormal Cells (CACs) Identification Using 4-Color Fluorescence In Situ Hybridization (FISH) Image and Deep Refined Learning. J Digit Imaging 2023;36:1687-700.
31. Xu X, Cong F, Chen Y, Chen J. Sleep Stage Classification With Multi-Modal Fusion and Denoising Diffusion Model. IEEE J Biomed Health Inform 2024. [Epub ahead of print]. doi: 10.1109/JBHI.2024.3422472.
32. Xu X, Li C, Fan X, Lan X, Lu X, Ye X, Wu T. Attention Mask R-CNN with edge refinement algorithm for identifying circulating genetically abnormal cells. Cytometry A 2023;103:227-39.
33. Zhang Y, Zhu W, Li K, Yan D, Liu H, Bai J, Liu F, Cheng X, Wu T. SMANet: multi-region ensemble of convolutional neural network model for skeletal maturity assessment. Quant Imaging Med Surg 2022;12:3556-68.
34. Wu J, Mi Q, Zhang Y, Wu T. SVTNet: Automatic bone age assessment network based on TW3 method and vision transformer. Int J Imaging Syst Technol 2024;34:e22990.

Cite this article as: Zhao H, Zhang Y, Zhang W, Wang L, Li K, Geng J, Cheng X, Wu T. An automatic deep learning-based bone mineral density measurement method using X-ray images of children. Quant Imaging Med Surg 2025;15(3):2481-2493. doi: 10.21037/qims-24-283